Engineering Structures 221 (2020) 111082

Contents lists available at ScienceDirect

Engineering Structures

journal homepage: www.elsevier.com/locate/engstruct

Compression tests of octagonal concrete-filled thin-walled tube columns

Jong-Jin Lim[a], Tae-Sung Eom[b,*]

[a] Senvex Co. Ltd, Beodeunaru-ro 19-gil, Yeongdeungpo-gu, Seoul 07226, Republic of Korea
[b] Dept. of Architectural Engineering, Dankook Univ., 152 Jukjeon-ro, Gyeonggi-do 448-701, Republic of Korea

ARTICLE INFO

Keywords:
Thin-walled tube
Octagonal tube
Compression test
Strain compatibility analysis
Composite column

ABSTRACT

The compression behavior of octagonal concrete-filled thin-walled tube (OCFT) columns was investigated. Eight OCFT columns with different tube sections were tested under monotonic compressive loading. The tests showed that the thin-walled tubes underwent elastic or inelastic local buckling, and the slenderness ratio (or width-to-thickness ratio) and section shape of the tubes significantly affected their buckling modes. Despite such local buckling, the load-deformation behavior of the OCFT columns all was highly ductile, due to confinement to the infilled concrete. The design strengths of AISC 360-16 agreed well with the test strengths. In this study, effective stress–strain relationships of the tube and infilled concrete were proposed to account for the local buckling and confinement. The maximum strength and post-buckling behavior were estimated through the strain-compatibility analysis, and the results were compared with the tests.

1. Introduction

Recently, the use of various types of filled composite (CFT) columns using thin-walled steel tubes has been growing. Such thin-walled tubes under compression may buckle easily before yielding, because the slenderness ratio λ (or width-to-thickness ratio) of the tube wall is relatively large. Basically, the buckling resistance and confining effect of the tube depend on the section shape and tube wall slenderness ratio. Compared to circular tubes, rectangular and square tubes are less efficient in resisting against elastic or inelastic local buckling, because the edges of the thin tube walls may not be fully clamped at the corners of the section [2,10,15,21]. Furthermore, after local buckling, confinement to the infilled concrete is less effective, because the out-of-plane stiffness of the thin tube wall is almost negligible.

The compressive strength and post-buckling behavior of square or rectangular CFT columns can be enhanced by placing stiffeners or rib plates on the tube wall, or by changing the square or rectangular section into polygonal sections. Tomii et al. [18] conducted the compression tests of circular, octagonal, and square columns with different tube wall slenderness ratios (width-to-thickness or diameter-to-thickness ratios) of λ = 19–75. The strength and ductility of the circular and octagonal columns were greater than those of the square columns. Ding et al. [4] assessed the performance of hexagonal and octagonal columns. Since the slenderness ratios of the tube walls were large, the compressive strength was degraded as buckling and yielding of the tubes occurred. However, as the tubes confined the infilled concrete, post-peak strength degradation was limited and consequently the post-buckling behavior was ductile. Ge and Usami [6] performed the compression tests of square tube columns with longitudinal rib plates on each side of the tube. As the rib plates reduced the slenderness ratio of the tube wall and consequently changed buckling modes, the column strength was increased. Tao et al. [17] investigated the buckling mode of stiffened thin-walled tube columns. The tube buckling mode and consequent compressive strengths of the columns agreed well with the theoretical ones. Due to the effects of local buckling, the column strength was significantly degraded during the post-buckling behavior. Huang et al. [7] investigated the compression behavior of square columns. To increase buckling resistance and confinement effect, the thin tube walls of the columns were stiffened by the tie bars placed diagonally at four corners. The tie bars were effective in increasing the compressive strength and ductility of the columns. The similar stiffening concept of using diagonal tie or link elements in CFT columns was also reported in Jamkhaneh et al. [8] and Jamkhaneh and Kafi [9]. Cai and He [3] used binding bars connecting two opposite tube walls in order to increase the confinement effect. The test results showed that the binding bars changed the buckling mode of the tube walls and provided additional confinement to the infilled concrete, and consequently the strength and ductility of the CFT columns were increased.

According to AISC 360-16, CFT columns using thin-walled tube sections are mostly classified into noncompact and slender sections, due to their large slenderness ratios. To accurately estimate the compressive behavior of such noncompact and slender CFT columns, it is necessary

* Corresponding author.
E-mail addresses: doublej17@naver.com (J.-J. Lim), tseom@dankook.ac.kr (T.-S. Eom).

https://doi.org/10.1016/j.engstruct.2020.111082
Received 16 October 2019; Received in revised form 2 July 2020; Accepted 4 July 2020

Nomenclature

A_c	area of the concrete infill
A_{cs}	area of the concrete infill confined by spiral reinforcement
A_{ct}	area of the concrete infill outside confining spirals
A_s	area of the steel tube
C_2	coefficient that accounts for confinement to the concrete infill by the steel tube
D_s	diameter of spiral reinforcement,
E_{spb}	post-buckling modulus of noncompact and slender steel tubes
E_s	modulus of elasticity of the steel tube or spiral reinforcement
F_{EXX}	tensile strength of weld metal
F_{cr}	buckling strength for steel tubes
F_y	yield stress of the steel tube
F_u	tensile strength of steel tubes
L	length of the OCFT column specimens
P	compressive load of CFT columns or compressive resistance at a given compressive strain ε of a CFT column section
P_{cr}	elastic buckling strength of CFT columns
P_{no}	nominal design strength of CFT columns without length effects
P_p	plastic strength of CFT columns
P_y	yield strength of CFT columns
P_u	maximum load of CFT columns by test
R	modified slenderness ratio of simply-supported plates
Δ	axial deformation (shortening) of OCFT column specimens
b	overall width of rectangular steel tubes
b_{eff}	effective width of the octagonal steel tube
d_b	diameter of reinforcing or spiral bars
f_c'	compressive strength of the concrete infill
f_{cc}'	enhanced compressive strength of the concrete infill due to confinement
f_l	effective lateral pressure f_l provided by the steel tube or spirals
f_y or f_{ys}	yield strength of reinforcing or spiral bars
f_u	tensile strength of reinforcing or spiral bars
k	buckling coefficient depending on the edge condition
s	spacing of spiral reinforcement
t	thickness of the steel tube
β_c	residual strength ratio of the concrete infill
δ	strength ratio of the steel tube to the CFT section ($=F_yA_s/[F_yA_s + 0.85f_c'A_c]$)
ε	compressive strain of the CFT column specimens ($=\Delta/L$)
ε_{bar}	tensile strain measured from the spiral bars
ε_{co}	strain at which the concrete compressive strength f_c' is reached
ε_{tube}	compressive strain measured from the steel tubes
$\varepsilon_{y,tube}$	yield strain of the steel tube ($=F_y/E_s$)
$\varepsilon_{y,tar}$	yield strain of the spiral bar ($=f_y/E_s$ or f_{ys}/E_s)
λ	slenderness ratio or width-to-thickness ratio of the steel tube
λ_p	slenderness ratio limit for compact/noncompact sections
λ_r	slenderness ratio limit for noncompact/slender sections
ν	Poisson's ratio of the steel tube
ρ	steel ratio of a CFT section ($=A_s/[A_s + A_c]$)
ρ_s	volume ratio of spiral reinforcement
σ_c	stress of the concrete infill
σ_{cs}	stress of the concrete infill confined by spiral reinforcement
σ_{ct}	stress of the concrete infill outside confining spirals
σ_s	stress of the steel tube

to account for the effects of local buckling and concrete confinement on strength and ductility. So far, various effective stress-strain relationships for the steel tube and filled concrete of CFT column sections that can be implemented in nonlinear fiber-based analysis were proposed. Sakino et al. [14] experimentally and analytically investigated the axial compressive behavior of short CFT columns. Based on the test results of 114 column specimens with different tube shapes, steel yield strength, tube wall slenderness ratios, and concrete compressive strengths, effective stress-strain relationships for the steel tube and filled concrete that accounted for the effects of tube local buckling and concrete confinement on the peak stress and post-peak degradation behavior of the materials were proposed. For the filled concrete in rectangular CFT columns, strength increase due to the confinement was neglected, whereas the ductility was assumed to be maintained by the confinement provided by the steel tubes. Liang et al. [12] proposed a nonlinear analysis method for concrete-filled thin-walled columns that accounted for the effects of local buckling. For the thin tube walls, the buckling strength incorporating the effects of initial imperfection and residual compressive stress was suggested and the post-buckling behavior was estimated based on the effective width approach [21,20]. Varma et al. [23] developed the effective stress-strain models of the steel tube and filled concrete for high-strength square CFT columns. Lai and Varma [11] proposed the effective stress-strain models for the steel tube and filled concrete of noncompact and slender CFT sections. Based on the results of comprehensive 3D finite element analyses, the effective stress-strain models for rectangular and circular CFT columns were developed in the form of uniaxial stress-strain relationships accounting implicitly for the effects of yielding and local buckling of the steel tubes and cracking and confinement of the filled concrete. The effective stress-strain models were implemented in a nonlinear fiber-based analysis, and the validity and conservatism of the models were verified by comparisons with the experimental database.

This study investigated the axial compressive behavior of octagonal CFT columns with thin-walled tubes. Eight octagonal CFT columns with different tube wall slenderness ratios and section shapes were tested under monotonic compressive loading. From the tests, buckling modes of the octagonal thin-walled tubes and consequent post-buckling behavior of the columns were investigated. The test strengths were compared with the design strengths of square and circular CFT sections in AISC 360-16. In addition, effective stress–strain models of the steel tubes and filled concrete that accounted for the effects of local buckling and confinement were proposed, and a strain compatibility analysis was performed using the proposed stress–strain relationships.

2. Test program

Fig. 1 shows the octagonal concrete-filled tube (OCFT) columns investigated in this study. Two types of octagonal steel tubes were used: Q-type and T-type tubes. The Q-type tube was made of four C-shaped plates, whereas the T-type tube was made of two C-shaped and two planar plates. Such octagonal tubes had the same section geometry as a square tube with chamfering; as the size of chamfering increases, the section geometry changes from a square to a regular octagon. Rib plates were used at the four corners to increase resistance against local buckling in the thin tube wall and reduce bond slip on the interface to the filled concrete. Compared to the conventional square CFT columns, the OCFT columns may have the slenderness ratio of the tube walls decreased and the section geometry closer to a regular octagon or a circle. As such, the section geometry of the OCFT columns was developed to enhance the compressive behavior of filled composite columns under axial load.

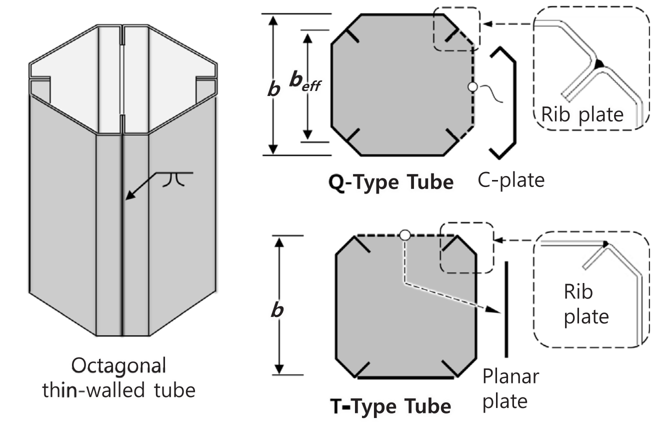

Fig. 1. Octagonal concrete-filled tube (OCFT) columns using thin-walled steel tubes.

2.1. Specimen details

Fig. 2 shows the details of eight OCFT column sections, Q4.5S, Q6.0S, T4.5S, T6.0S, T6.0S-75, T6.0S-150, T4.5R, and T6.0R. In the specimen names, 'Q' and 'T' indicate the Q-type and T-type tubes, respectively; '4.5′ and '6.0′ indicate the thickness of the tube walls; and 'S' and 'R' indicate the section geometry of the octagonal tubes close to square and regular octagon, respectively. Table 1 summarizes these test variables.

For Q4.5S (t = 4.5 mm) and Q6.0S (t = 6.0 mm), the Q-type tubes were used (see Fig. 2(a)). The overall width of the steel tubes was b = 400 mm, while the effective width, defined as the distance between the rib plates at the adjacent corners, was b_{eff} = 316 mm. Note that for square tubes, the slenderness ratio λ (or width-to-thickness ratio) accounting for local buckling needs to be computed using the inner dimension (AISC 360-16). Thus the slenderness ratios were $\lambda = (b - 2t)/t = 86.9$ and $\lambda_{eff} = (b_{eff} - 2t)/t = 68.2$ for Q4.5S, and $\lambda = (b - 2t)/t = 64.7$ and $\lambda_{eff} = (b_{eff} - 2t)/t = 50.7$ for Q6.0S (see Table 1). For T4.5S (t = 4.5 mm) and T6.0S (t = 6.0 mm), the T-type tubes were used (see Fig. 2(b)). The effective width was the same as the overall width (i.e. $b = b_{eff}$ = 400 mm), and thus the slenderness ratio was $\lambda = \lambda_{eff} = (b - 2t)/t = 86.9$ for T4.5S, and 64.7 for T6.0S (see Table 1).

For T6.0S-75 and T6.0S-150, the T-type tubes with a tube wall thickness of t = 6 mm were used, and the slenderness ratio was $\lambda = \lambda_{eff} = (b - 2t)/t = 64.7$ (see Fig. 2(c) and Table 1). Inside the steel tubes, the spiral reinforcement made of D10 bars (diameter d_b = 9.5 mm) was additionally placed. The spacing of the spiral reinforcement was s = 75 mm for T6.0S-75, and 150 mm for T6.0S-150. The diameter of the spiral hoops was D_s = 300 mm. The volume ratio of the spiral reinforcement was ρ_s = 1.26% for T6.0S-75, and 0.63% for T6.0S-150. The spiral reinforcement was used to provide additional confinement to the concrete infill.

For T4.5R (t = 4.5 mm) and T6.0R (t = 6.0 mm), the T-type tubes were used (see Fig. 2(d)). Unlike other specimens where the section geometry of the octagonal tubes was close to a square, the section geometry of the octagonal tubes in T4.5R and T6.0R was close to a regular octagon. The width of the sides in the octagonal section was 156 mm and 180 mm.

Table 1 shows the section classification of the OCFT columns. For the octagonal tubes similar to a square (i.e. Q4.5S, Q6.0S, T4.5S, T6.0S, T6.0S-75, and T6.0S-150), the sections were classified based on the limits of slenderness ratio, λ_p and λ_r, for square tubes (AISC 360–16). Q4.5S and Q6.0S were classified as slender and noncompact sections, respectively, regardless of judgment either by λ (= b/t) or λ_{eff} (= b_{eff}/t). T4.5S was classified as slender section, whereas T6.0S, T6.0S-75, and T6.0S-150 were classified as noncompact sections. T4.5R and T6.0R of a regular octagon were classified as slender and compact sections, respectively, based on λ_p and λ_r for circular tubes.

Table 1 also shows the steel area A_s, concrete area A_c, steel ratio ρ, and strength ratio δ. The steel ratio and strength ratio were defined as $\rho = A_s/(A_s + A_c)$ and $\delta = F_yA_s/(F_yA_s + 0.85f_c'A_c)$, respectively ($F_y$ = yield strength of the steel and f_c' = compressive strength of the concrete). The steel ratios ρ ranged 4.71% to 7.15%. Such steel ratios were relatively low, compared with those of conventional CFT columns. The strength ratios δ ranged 46.3–52.8%, which indicates that the contributions of the steel and concrete to the compressive strength were almost the same.

2.2. Material strength

Thin steel plates of thickness 4.5 mm and 6.0 mm were used for the steel tubes of the OCFT columns. The yield and ultimate strengths were F_y = 489 MPa and F_u = 527 MPa for the 4.5 mm thick plates, and F_y = 407 MPa and F_u = 557 MPa for the 6.0 mm thick plates. For welding, weld metal of F_{EXX} = 560 MPa was used. Note that when steel plate undergoes plastic deformation by press bending, the yield strength in the bent zone (i.e. the corners of the section) can increase, due to strain hardening. Thus the welded joint that is located in the bent zone can be more sensitive to early rupture. However, according to Tao et al. [17], Huang et al. [7], and Cai and He [3], the behavior of concrete-filled thin-walled tube columns is mainly dominated by local buckling, rather than by rupture at the welded joint.

For D10 bars of diameter d_b = 9.5 mm, used for the spiral reinforcement in T6.0S-75 and T6.0S-150, the yield and ultimate strengths were f_y = 486 MPa and f_u = 563 MPa, respectively.

For the infilled concrete, three concrete cylinders of diameter 100 mm and height 200 mm were tested under pure compressive loading. The mean concrete strength was f_c' = 33.0 MPa.

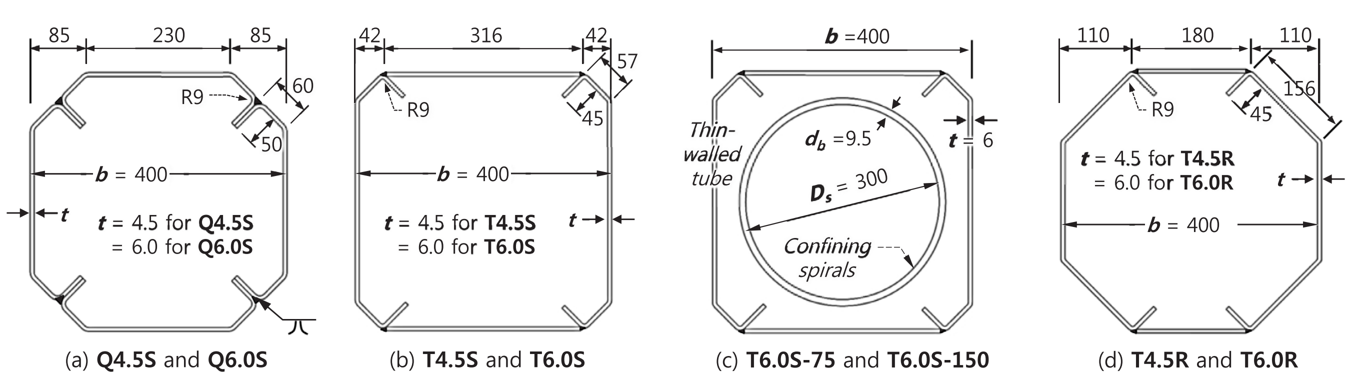

Fig. 2. Details of octagonal tube column specimens (mm).

Table 1
Test parameters.

Specimens	t (mm)	$\lambda = (b–2\,t)/t$	$\lambda_{eff} = (b_{eff} –2t)/t$ or D/t	λ_p 1)	λ_r 1)	Section Classification	A_s (mm^2)	A_c (mm^2)	Steel ratio ρ (%) 3)	Strength ratio δ (%) 3)
Q4.5S	4.5	86.9	68.2	45.7	60.7	Slender	7,790	137,830	5.35	49.6
Q6.0S	6.0	64.7	50.7	50.0	66.4	Noncompact	10,400	134,980	7.15	52.8
T4.5S	4.5	86.9	86.9	45.7	60.7	Slender	7,380	149,360	4.71	46.3
T6.0S	6.0	64.7	64.7	50.0	66.4	Noncompact	9,820	146,430	6.28	49.3
T6.0S-75	6.0	64.7	64.7	50.0	66.4	Noncompact	9,820	146,430	6.28	49.3
T6.0S-150	6.0	64.7	64.7	50.0	66.4	Noncompact	9,820	146,430	6.28	49.3
T4.5R	4.5	88.9	88.9	61.3	77.7	Slender 2)	6,710	129,090	4.94	47.5
T6.0R	6.0	66.6	66.6	73.5	93.1	Compact 2)	8,950	129,850	6.45	50.0

1) For Q4.5S, Q6.0S, T4.5S, T6.0S, T6.0S-75, and T6.0S-150, $\lambda_p = 2.26\sqrt{(E_s/F_y)}$ and $\lambda_r = 3.0\sqrt{(E_s/F_y)}$. For T4.5R and T6.0R, $\lambda_p = 0.15E_s/F_y$ and $\lambda_r = 0.19E_s/F_y$ (E_s = 200,000 MPa).
2) The section classification was based on the criteria for circular tubes.
3) The steel ratio and strength ratio were computed as $\rho = A_s/(A_s + A_c)$ and $\delta = F_yA_s/(F_yA_s + 0.85f_c'A_c)$.

2.3. Fabrication and test setup

Fig. 3 shows the octagonal steel tube under fabrication. The steel tubes were made by press bending and welding (see Figs. 1 and 2). For welding, the weld size was greater than the thickness of the plates. During the fabrication, deformation due to welding was not significant.

Fig. 4(a) shows the test setup for OCFT columns under compressive loading. End plates of 600 mm × 600 mm × 40 mm were used at the top and bottom. To prevent stress concentration near the welded joint between the tube and end plate, vertical stiffeners (thickness 12 mm) were used. In addition, 8 headed studs (diameter 22 mm) were also used, so that from the beginning, axial loads could be applied to both the steel tube and infilled concrete at the same time. Axial loads were monotonically applied by controlling vertical displacement, and the loading speed (=0.003 mm/s) was maintained sufficiently slow.

Fig. 4(b) shows the locations of the strain gauges used for the steel tubes and spiral bars. For the steel tubes, six or five strain gauges were installed at mid-height in the longitudinal direction. For the spiral bars, a strain gauge was installed in the transverse direction.

3. Test results

3.1. Axial load–deformation relationships

Fig. 5 shows the axial load–strain (P–ε) relationships. The horizontal axis indicates the average axial strain over the net column length (L = 1200 mm). The maximum loads P_u are denoted with circles.

For Q4.5S and Q6.0S using Q-type tubes (see Fig. 5(a)), the overall P–ε behavior was similar. Although the steel tubes were subjected to local buckling, the post-buckling behavior was highly ductile. The strength was greater in Q6.0S (P_u = 8714 kN) using the 6 mm thick tube, than in Q4.5S (P_u = 7,197 kN) using the 4.5 mm thick tube.

For T4.5S and T6.0S using T-type tubes (see Fig. 5(b)), the overall P–ε behavior was similar to that of Q4.5S and Q6.0S. The strengths of T4.5S and T6.0S were about 10% less than those of Q4.5S and Q6.0S, respectively. Although the steel tubes were subjected to local buckling, the post-buckling behavior was very ductile. Note that the maximum loads of T4.5S and T6.0S occurred immediately after compressive yielding. This shows the section geometry of the T-type tubes in T4.5S and T6.0S (i.e. close to square) were not less efficient in resisting local buckling and consequently developing confinement to the filled concrete.

For T6.0S-75 and T6.0S-150 using T-type tubes and spiral reinforcement (see Fig. 5(c)), the initial behavior before yielding was similar to that of T6.0S. However, as the spiral reinforcement provided additional confinement to the infilled concrete, post-yield hardening behavior followed. Consequently, the maximum loads, P_u = 8213 kN and 7969 kN, respectively, occurred during the post-yield hardening behavior. Note that the use of the spiral reinforcement did not significantly increase the strengths of T6.0S-75 and T6.0S-150, compared to T6.0S, which indicates that the contribution of the spiral reinforcement was limited.

For T4.5R and T6.0R using regular octagon tubes (see Fig. 5(d)), the overall P–ε behavior including the post-yield hardening behavior was similar to that of T6.0S-150. The maximum loads of T4.5R and T6.0R were P_u = 6707 kN and 8064 kN, respectively. Such strengths were greater than those of T4.5S and T6.0S with the section geometry close to square, though the steel and concrete areas were about 10% less (see Table 1).

3.2. Failure modes

Fig. 6 shows the buckling modes of the octagonal steel tubes. For Q4.5S and Q6.0S, as shown in Fig. 6(a) and (b), local buckling of the steel tubes occurred separately on each side. There was no buckling at the chamfered corners, as the rib plates embedded within the infilled concrete provided lateral support. Locations of local buckling, highlighted by the white lines, were reduced by half in Q6.0S. For T4.5S and T6.0S (see Fig. 6(c) and (d)), the area of local buckling on each side in the T-type tubes was interconnected through the chamfered corners. This indicates that the 135° bend at the corners was not stiff enough to restrain local buckling on one side from propagating into other sides. Similar buckling modes were observed in T6.0S-75 and T6.0S-150 using the same T-type tube as that of T6.0S. For T4.5R and T6.0R using regular octagon tubes (see Fig. 6(e) and (f)), the areas of local buckling on eight sides occurred almost at the same height, and were interconnected with each other.

Buckling modes in Fig. 6 indicate that for the OCFT columns, the slenderness ratio (λ) needs to be defined differently, depending on the type and section geometry of the steel tubes, as follows:

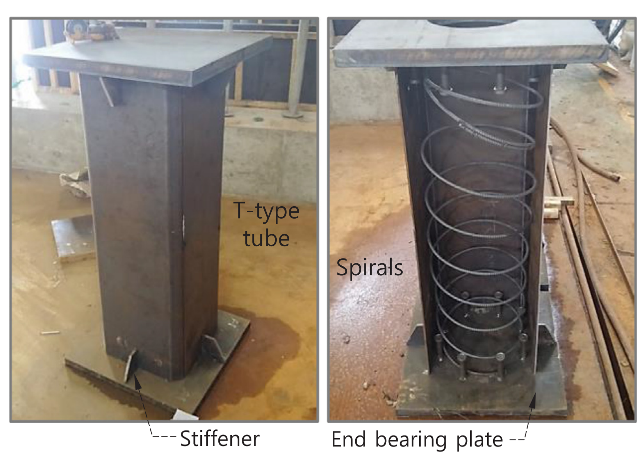

Fig. 3. Fabrication of octagonal steel tube.

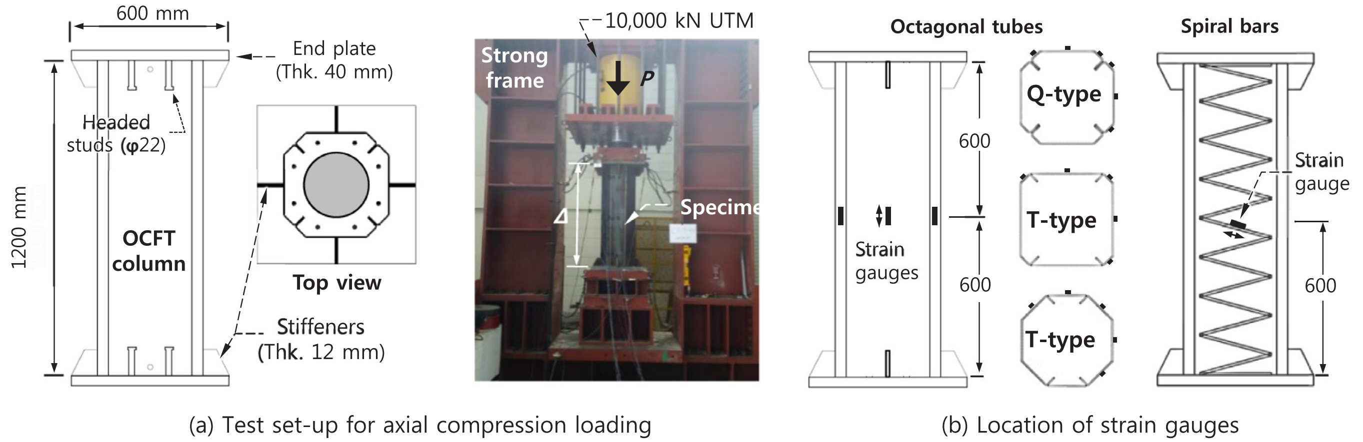

Fig. 4. Test setup of column specimens and locations of strain gauges.

- For Q-type tubes where the rib plates embedded with the infilled concrete at the corners provide sufficient lateral support against local buckling, λ can be defined using the distance between the rib plates (see Fig. 1).
- For T-type tubes, λ should be determined based on the overall tube dimension b, regardless of whether the section geometry is close to square or regular octagon. Note that OCFT columns have different buckling modes of the steel tubes depending on the section geometry. If the section geometry is close to square the buckling mode of the octagonal tube is similar to those of rectangular or square tubes. On the other hand, if the section geometry is close to regular octagon square the buckling mode of the octagonal tube is similar to those of circular tubes.

3.3. Strains of steel tubes

Fig. 7 shows the axial load–tube wall strain (P–ε_{tube}) relationships. The tube wall strains ε_{tube} were measured from the six or five strain gauges installed in mid-height (see Fig. 4). For Q4.5S, the P–ε_{tube} relationships were not uniform from the beginning. This means that the steel tube in Q4.5S had initial imperfection, or buckled heavily around the locations where the strains were acquired. Considering initial imperfection was inevitable in the thin-walled tubes, the moment and location at the onset of local buckling were hardly detected by visual inspection. Thus the initiation of local buckling in the tube walls were identified from the strain measurement, as follows.

For Q4.5S and T4.5S classified as slender sections (see Fig. 7(a) and (c)), the maximum strengths occurred around ε_{tube} = 0.0015–0.002 mm/mm before yielding ($\varepsilon_{y,tube}$ = 0.00245 mm/

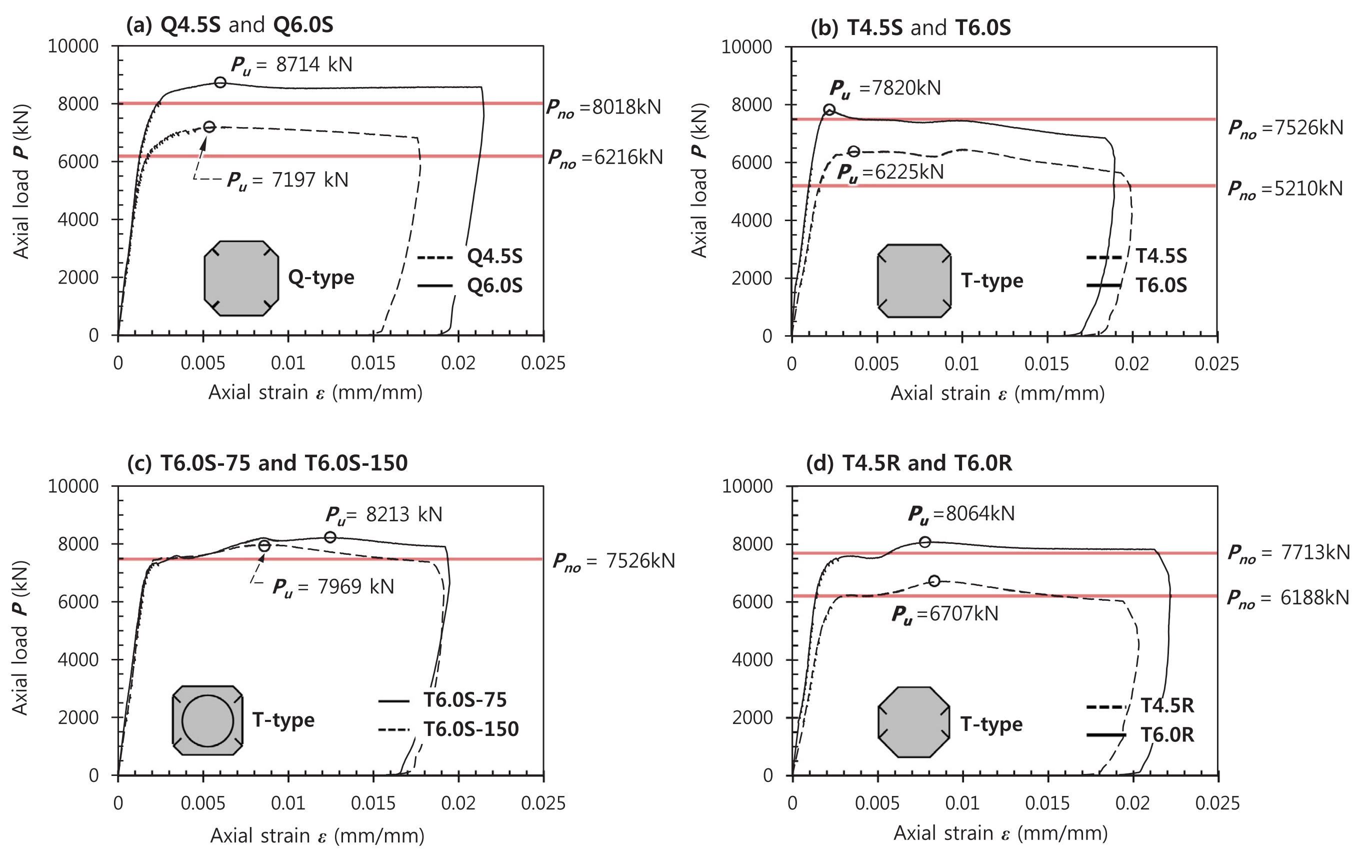

Fig. 5. Axial load-strain (P-ε) relationships.

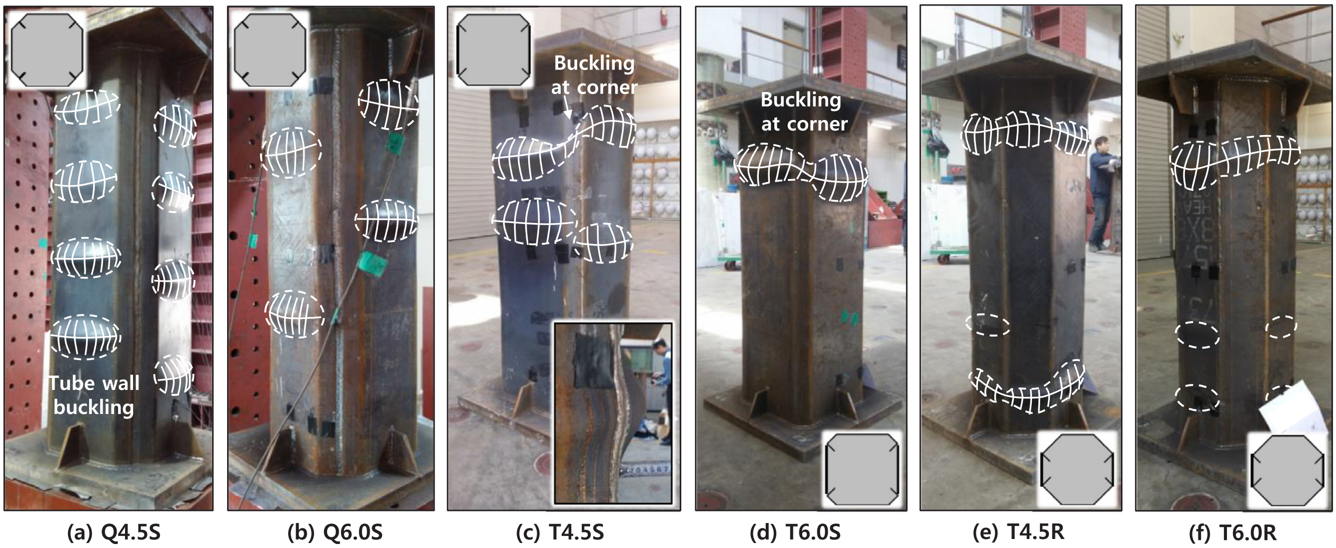

Fig. 6. Local buckling of octagonal tubes.

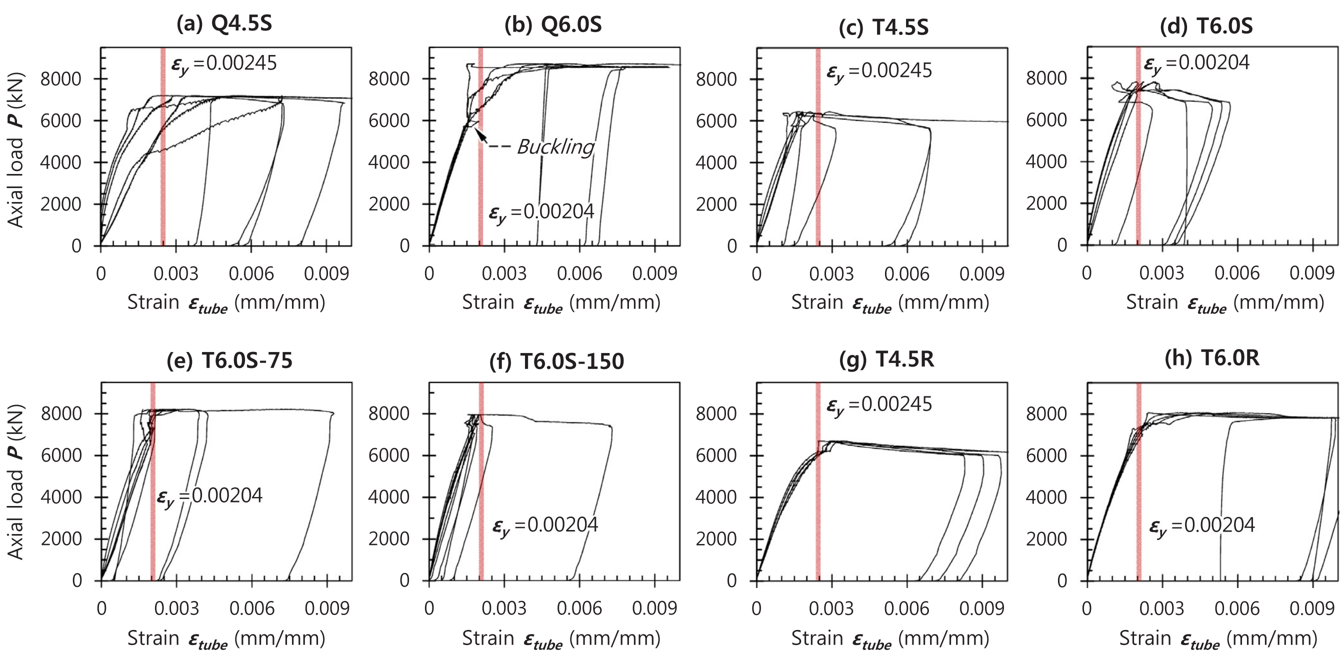

Fig. 7. Strains of octagonal tubes.

mm). This indicates that the steel tubes were subjected to elastic local buckling. On the other hand, for Q6.0S and T6.0S classified as non-compact sections (see Fig. 7(b) and (d)), the maximum strengths occurred soon after ε_{tube} reached the yield strain. The P–ε_{tube} curves displayed irregular patterns just before the yield strain, which indicates that local buckling occurred at that point. For T6.0S-75 and T6.0S-150, the P–ε_{tube} curves were similar to those of T6.0S.

For T4.5R and T6.0R using regular octagon tubes, all P–ε_{tube} curves displayed the same pattern. This might be because local buckling was less significant at the mid-height where the strains ε_{tube} were measured (see Fig. 6(e) and (f)). Note that, although T4.5S and T4.5R both used T-type tubes, only T4.5R with the section geometry close to regular octagon had the strength increasing almost linearly up to the yield strain, $\varepsilon_{y,tube}$ = 0.00245 mm/mm. This indicates that the regular octagon tube in T4.5R was more efficient in resisting local buckling, than the steel tube in T4.5S with the section geometry close to a square.

3.4. Comparison of the strains of steel tube and spiral bar

Fig. 8 compares the strains of the spiral bars (f_y = 486 MPa) and tube walls (F_y = 407 MPa), ε_{bar} and ε_{tube}, used for T6.0S-75 and T6.0S-150. Solid and dashed lines indicate the variations of ε_{tube} and ε_{bar}, respectively, with increasing column axial strain ε. ε_{bar} was tensile strain in the transverse direction, whereas ε_{tube} was compressive strain in the longitudinal direction. The strain ε_{tube} in Fig. 8(a) and (b) was the same as the largest strain in Fig. 7(e) and (f), respectively. For comparison, the axial load-strain (P-ε) relationships are also presented in Fig. 8, and based on these P-ε relationships, three divisions of the elastic, hardening, post-peak degradation zones are divided with the vertical lines and shades. As shown in Fig. 8, the points where the tube walls and spiral bars reached their yield strains differed, as follows. The tube walls reached their yield strain $\varepsilon_{y,tube}$ (= 407 MPa/200 GPa = 0.00204 mm/mm) early at the points where the columns began to yield ($\varepsilon \fallingdotseq 0.002$ mm/mm), whereas the spiral bars reached their yield strain $\varepsilon_{y,bar}$ (= 486 MPa/200 GPa = 0.00243 mm/mm) roughly at

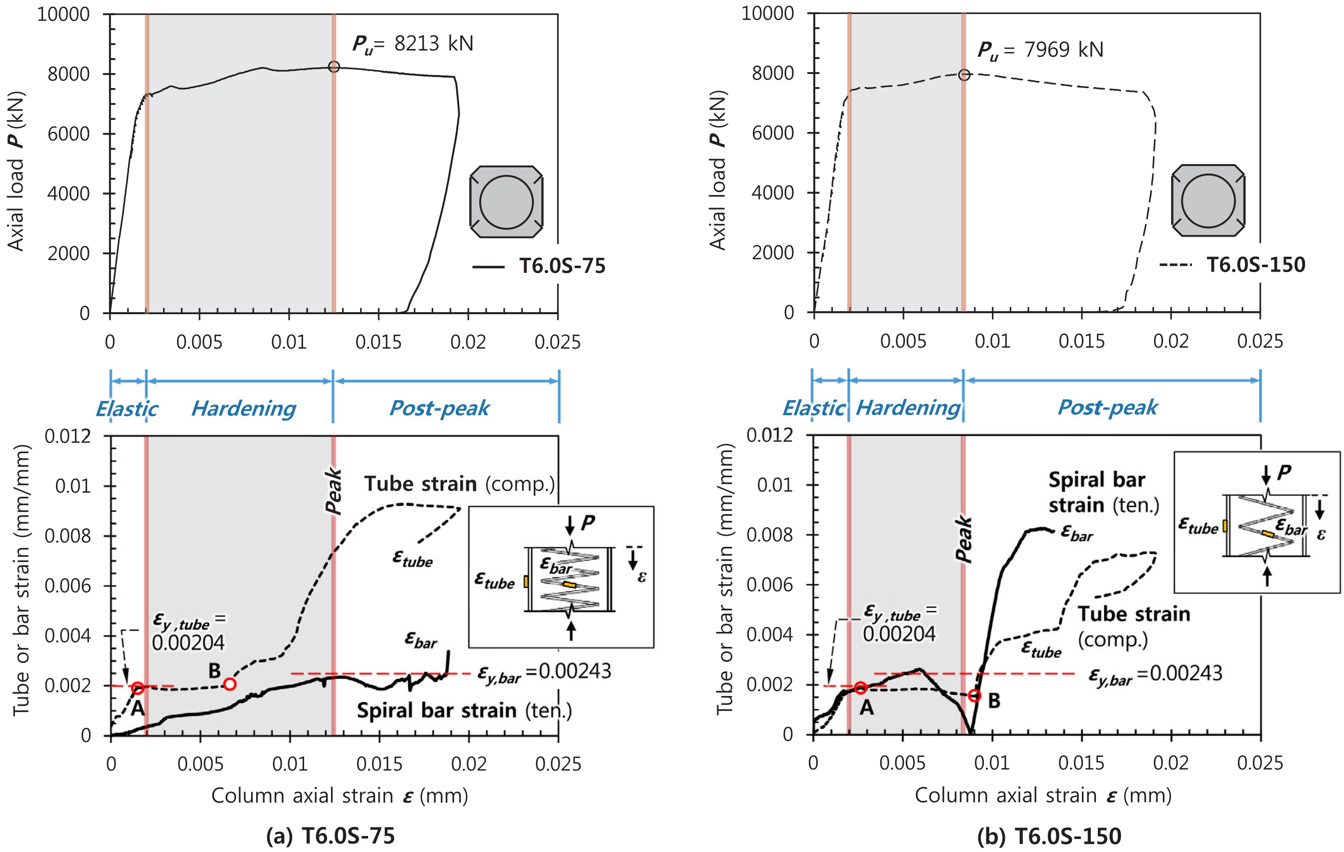

Fig. 8. Comparison of the strains of tube wall and spiral bar varying with column axial strain.

the points where the columns reached their peak strengths.

In Fig. 8(a) and (b), the hardening zones where the strength gradually increased from the yielding point to the peak point are denoted as shaded areas. The strains of the spiral bars, ε_{bar}, in the hardening zones increased up to the yield strain. In particular for T6.0S-75 with a spiral reinforcement ratio of $\rho_s = 1.26\%$, ε_{bar} increased slowly, and as a result the hardening zone lasted until $\varepsilon = 0.0123$ mm/mm. This indicates that the hardening behavior in T6.0S-75 was attributed to the concrete confinement by the spiral reinforcement. The strain of the tubes, ε_{tube}, remained constant at roughly $\varepsilon_{y,tube}$ between points A and B, which means that between points A and B, the tubes underwent local buckling in other locations.

During the post-peak behavior where the compression strength was degraded slowly, ε_{tube} and ε_{bar} increased beyond the yield strains. This indicates that during such degradation behavior, the infilled concrete underwent significant dilation, and consequently the strains of the steel tubes and spiral bars confining the infilled concrete increased.

4. Strain-compatibility analysis

A strain-compatibility analysis was performed to investigate the axial compressive behavior of the OCFT columns with different tube wall thickness and section shape.

For a given axial strain ε, the compressive resistance $P(\varepsilon)$ of an OCFT column can be computed as follows (see Fig. 9(a)):

$$P(\varepsilon) = \sigma_s(\varepsilon)A_s + \sigma_c(\varepsilon)A_c \tag{1}$$

where σ_s, σ_c, A_s, and A_c are the stresses and areas of the steel and infilled concrete. If spiral reinforcement is used inside the steel tube (refer to Fig. 5(c)), the concrete confined by the spiral reinforcement may have

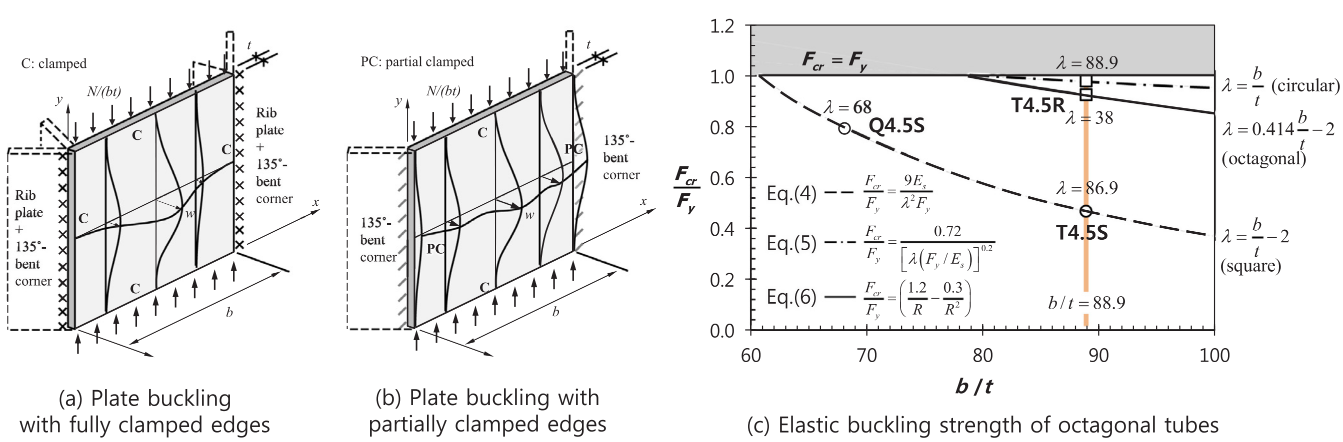

Fig. 9. Bucking mode and strength of octagonal tube.

different mechanical properties. In this case, $P(\varepsilon)$ needs to be modified as follows:

$$P(\varepsilon) = \sigma_s(\varepsilon)A_s + [\sigma_{ct}(\varepsilon)A_{ct} + \sigma_{cs}(\varepsilon)A_{cs}] \quad (2)$$

where σ_{cs} and A_{cs} are the stress and area of the concrete confined by the spiral reinforcement, respectively, and σ_{ct} and A_{ct} are the stress and area of the concrete in the remaining portion, respectively.

The stresses of the steel and concrete components accounting for the effects of local buckling and confinement (i.e. σ_s, σ_c, σ_{ct}, and σ_{cs}) are determined from the effective stress–strain relationships as follows.

4.1. Local buckling and effective stress–strain relationships of octagonal tubes

Fig. 9 shows the buckling mode of a tube wall (i.e. on each side) in octagonal tubes, depending on the clamping condition at both edges. If the tube wall subjected to uniform compressive stress is fully clamped at both edges by the rib plates embedded within the infilled concrete, the thin tube wall buckles independently, and consequently the buckling load increases (see Fig. 9(a)). On the other hand, for the tube wall where its edges are partially clamped by 135° bend corners (see Fig. 9(b)), local buckling of the adjacent tube walls is interconnected, and consequently the buckling load decreases. According to Uy and Bradford [22], Uy [21], and Trahair et al. [20], the buckling strength of the tube wall can be expressed as follows:

$$F_{cr} = \frac{k\pi^2 E_s}{12(1-\nu^2)\lambda^2} \quad (3)$$

where k = buckling coefficient depending on the edge conditions; E_s = modulus of elasticity of the steel tube (=200,000 MPa); ν = Poisson's ratio of the steel tube (=0.3); and λ = slenderness ratio of the tube wall. In Eq. (3), k is taken as 5.2 if the longitudinal edges are pinned, and as 10.3 if the longitudinal edges are fixed [22].

The buckling strength for square tubes, F_{cr} ($=9E_s/\lambda^2$), adopted by AISC 360–16, is the same as the strength computed by substituting k = 10.3. For the octagonal tubes investigated in this study, it is difficult to define a constant buckling coefficient: where both edges of the tube wall are fully clamped by the rib plates, k = 10.3 can be used; whereas, where one or both edges are partially clamped by 135° bend corners, a smaller k needs to be used (see Fig. 9). Furthermore, considering that each tube wall has different width (refer Fig. 2), it is inconvenient to define F_{cr} for individual tube walls. Thus in this study, F_{cr} for square tubes in AISC 360–16 is used as the elastic buckling strength for the octagonal tubes with the section geometry similar to square.

$$F_{cr} = \frac{9E_s}{\lambda^2} \text{ for octagonal tubes with section geometry similar to square} \quad (4)$$

where $\lambda = (b_{eff} - 2\,t)/t$ and b_{eff} is the effective width of the tube. As discussed in Failure modes, buckling modes differ in the Q-type and T-type tubes. For the T-type tubes (i.e. T4.5S and T6.0S), b_{eff} is taken as the overall tube dimension (=b); on the other hand, for the Q-type tubes (i.e. Q4.5S and Q6.0S), b_{eff} is taken as the distance between the rib plates at the adjacent corners (see Fig. 1).

For regular octagon tubes (i.e. T4.5R and T6.0R), the buckling strength increases as buckling mode becomes similar to that of circular tubes (see the buckling modes of the tubes walls in Fig. 6(e) and (f)). The buckling strengths of octagonal and circular tubes can be calculated as follows [2,16]:

$$F_{cr} = \frac{0.72F_y}{[\lambda(F_y/E_s)]^{0.2}} \text{ for circular tubes} \quad (5)$$

$$F_{cr} = \left(\frac{1.2}{R} - \frac{0.3}{R^2}\right)F_y \text{ for regular octagon tubes} \quad (6)$$

where R is the modified slenderness ratio for simply-supported plates, defined as follows [16,20]:

$$R = \lambda\sqrt{\frac{12(1-\nu^2)}{4\pi^2}\frac{F_y}{E_s}} \quad (7)$$

Note that Eq. (5) is the AISC 360-16 equation for circular columns, and λ is defined as b/t. For Eqs. (6) and (7) based on the buckling theory of individual plates on each side of the octagonal tube, λ is defined as $(b_{eff} - 2\,t)/t$, where b_{eff} is the largest width of flat tube walls. For regular octagon tubes, $b_{eff} = (\sqrt{2} - 1)b = 0.414b$.

Fig. 9(c) compares the buckling strengths F_{cr} of square, octagonal (i.e. regular octagon), and circular tubes depending on b/t (F_y = 487 MPa). For a given b/t, the F_{cr} –b/t curves are plotted using $\lambda = (b–2t)/t$ for square tubes (Eq. (4)), $\lambda = (0.414b–2t)/t$ for octagonal tubes (Eq. (6)), and $\lambda = b/t$ for circular tubes (Eq. (5)). The buckling strengths F_{cr} of circular and octagonal tubes are significantly greater than that of square tubes. In particular for thin-walled tubes of $b/t > 80$, the elastic local buckling strength F_{cr} is greater in the order of square, octagonal, and circular tubes. Considering that the buckling resistance highly depends on the section shape, such strength hierarchy is reasonable. Fig. 9(c) plots the buckling strengths of the Q-type and T-type tubes (t = 4.5 mm thickness) used for Q4.5S, T4.5S, and T4.5R. Although both Q4.5S and T4.5S use Eq. (4), F_{cr} of Q4.5S computed using the effective width b_{eff} (λ = 68.0, refer to Fig. 1) is significantly greater than that of T4.5S using the overall width b (λ = 86.9). For the regular octagon tube of T4.5R using Eq. (6) (λ = 38.0), the buckling strength becomes almost two times F_{cr} of T4.5S.

Once the buckling strength F_{cr} of the steel tubes is determined from Eqs. (4) and (6), the effective stress–strain relationships of octagonal tubes accounting for local buckling under compressive loading can be idealized as follows (see Fig. 10):

- For $F_{cr} < F_y$ (see Fig. 10(a)):

Before local buckling occurs, the stress of the steel tube, σ_s, increases up to F_{cr}, with increasing ε. Local buckling occurs at $\varepsilon = \varepsilon_{cr}$ (or $\sigma_s = F_{cr}$), and then it is assumed that σ_s decreases linearly with increasing ε, with a post-buckling modulus E_{spb}.

- For $F_{cr} \geq F_y$ (see Fig. 10(b)):

Since F_{cr} is greater than the yield strength F_y, yielding of the tube occurs before local buckling. In this case, σ_s increases up to F_y. If the steel tube is a noncompact section, σ_s is assumed to decrease linearly from F_y with E_{spb} as ε increases. On the other hand, if the steel tube is a compact section, σ_s is assumed to remain constant at F_y.

For thin-wall tubes, the load-carrying capacity is maintained or increases with increasing deformation even after local buckling, as stresses are redistributed from the heavily buckled central region to the edge or corner region [20,12,21]. For the octagonal tubes investigated in this study, the rib plates embedded within the infilled concrete can also contribute to the post-buckling strength. The post-buckling

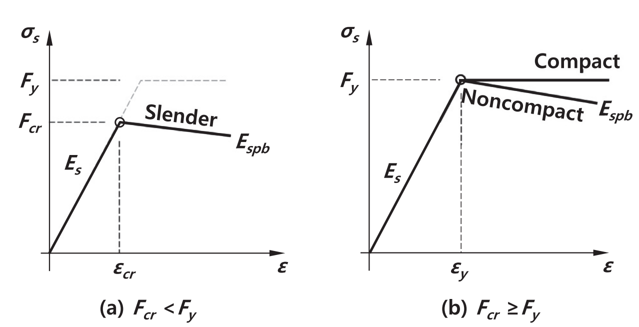

Fig. 10. Effective stress–strain relationships of steel tube accounting for local buckling.

behavior of the octagonal tubes can be investigated in detail based on the effective width approach [20,12]. However, considering the buckling strength and stress–strain relationships in Fig. 10 are established based on the average stresses and strains for the whole tube section, the effective width approach may not be appropriate.

In this study, to account for a gradual deterioration behavior after elastic or inelastic local buckling, the effective stress–strain behavior of the octagonal tubes is idealized as a bilinear relationship with a post-buckling modulus. The post-buckling modulus was approximated as $E_{spb} = 0.03E_s$, based on the existing models by Sakino et al. [14] and Lai and Varma (2005) [11] as follows. Sakino et al. [14] and Lai and Varma (2005) [11] proposed simple and straightforward models for the steel tubes of rectangular and circular CFT columns, based on the 114 CFT short column tests and the comprehensive 3D finite element analyses of CFT columns with a wide range of geometrical and material properties. According to the Lai and Varma's model, the post-buckling behavior of rectangular and circular tubes under compressive loading is approximated as trilinear and bilinear curves, respectively. For rectangular steel tubes, the decrease in the steel stress after local buckling on the descending branch stops at two times the steel yield strain, and then the steel stress is maintained constant. On the other hand, for circular tubes, the post-buckling deterioration is negligible, and thus the stress-strain behavior of the steel is idealized as elastic-perfectly plastic. For the OCFT columns investigated in this study, Q4.5S, Q6.0S, T4.5S, T6.0S, T6.0S-75, and T6.0S-150 have octagonal tubes with the section geometry close to square, whereas T4.5R and T6.0R have octagonal tubes with the section geometry close to circle. Thus, for consistent modeling of the octagonal tubes, a bilinear model with a post-buckling modulus of $E_{spb} = 0.03E_s$ is applied for noncompact and slender tube sections, regardless of the section geometry.

4.2. Effective stress–strain relationships of infilled concrete

For the infilled concrete confined by square tubes, strength increase due to confinement is limited. Thus, for the octagonal tubes with the section geometry similar to a square, a simplified stress–strain (σ_c-ε) relationship proposed by Tomii and Sakino [19] is used (see Fig. 11(a)). In this σ_c–ε relationship, strength increase due to confinement is ignored; instead, the ductility and residual strength are significantly increased, as follows:

$$\sigma_c(\varepsilon) = \begin{cases} f_c'\left[2\left(\frac{\varepsilon}{\varepsilon_{co}}\right) - \left(\frac{\varepsilon}{\varepsilon_{co}}\right)^2\right] \text{ for } \varepsilon \leqslant \varepsilon_{co} \\ f_c' \text{ for } \varepsilon_{co} < \varepsilon \leqslant 0.005 \\ f_c' - (1-\beta_c)f_c'\ (1.5 - 100\varepsilon) \text{ for } 0.005 < \varepsilon \leqslant 0.015 \\ \beta_c f_c' \text{ for } 0.015 < \varepsilon \end{cases} \tag{8}$$

where $\sigma_c(\varepsilon)$ = stress of the concrete varying with ε; ε_{co} = strain at which the compressive strength f_c' is reached (=0.002 mm/mm); and β_c ($\leq$1.0) = residual strength ratio. β_c depends on design parameters, such as the shape and b/t ratio of the steel tube. For the OCFT columns, the strength degradation after local buckling was negligible, and rather increased due to hardening, as shown in Fig. 5. Thus in this study, β_c = 0.85 is used.

For OCFT columns with regular octagon tubes, the strength of the infilled concrete can increase due to confinement (refer to Fig. 5(d)). Thus, the stress–strain curve of such infilled concrete can be defined using Eq. (8) by replacing f_c' with f_{cc}'. The enhanced concrete strength due to confinement, f_{cc}', is determined using the effective lateral pressure f_l, as follows [5,16].

$$f_{cc}' = f_c' + 3.7f_l \tag{9}$$

$$f_l = -35R\frac{f_c'^{1.35}}{F_y} + 0.22f_c'^{1.02} \text{ for regular octagon tubes} \tag{10}$$

In Eq. (10), f_l is taken as zero for $R > 0.85$, because if the slenderness ratio (or width-to-thickness ratio) is large, the strength increase due to the confinement vanishes [16].

For the concrete confined by spiral reinforcement, both the strength and ductility increase. For such confined concrete, the stress–strain curve proposed by Mander et al. [13] is used as follows (see Fig. 10(c)):

$$\sigma_c(\varepsilon) = f_{cc}'\frac{xr}{r-1+x^r} \tag{11}$$

where f_{cc}' = compressive strength of the confined concrete (see Eq. (9)); f_l = effective lateral pressure due to confinement; $\varepsilon_{cc} = \varepsilon_{co}[f_{cc}'/f_c']^2$; $x = \varepsilon/\varepsilon_{cc}$; $r = E_c/[E_c - E_{sec}]$; E_c = elastic modulus of concrete (=4500√f_c'); and E_{sec} = secant modulus at the peak point (=f_{cc}'/ε_{cc}). For the concrete confined by the spiral reinforcement, f_l is defined as follows [5]:

$$f_l = \frac{1}{2}\rho_s f_{ys}\left(1 - \frac{s}{D_s}\right) \text{ for spiral reinforcement} \tag{12}$$

where ρ_s = spiral reinforcement ratio; f_{ys} = yield strength of spiral bars; and s and D_s = spacing and diameter of the spiral reinforcement, respectively.

4.3. Results of strain-compatibility analysis

Fig. 12 shows the results of strain compatibility analyses for eight OCFT column specimens. The results of the analysis and test are denoted as solid and dashed lines, respectively. The analysis was performed using the effective stress–strain relationships proposed in the previous section (see Figs. 10 and 11). For comparison, the plastic strength P_p, yield strength P_y, and elastic buckling strength P_{cr}, specified in AISC 360-16, are also represented as horizontal solid, dotted, and dashed lines, respectively. P_p, P_y, and P_{cr} are computed as follows:

$$P_p = A_sF_y + C_2A_cf_c' \tag{13}$$

$$P_y = A_sF_y + 0.7A_cf_c' \tag{14}$$

$$P_{cr} = A_sF_{cr} + 0.7A_cf_c' \tag{15}$$

For 4.5S, Q6.0S, T4.5S, T6.0S, T6.0S-75, and T6.0S-150, C_2 = 0.85 was used in Eq. (13), and F_{cr} ($\leq F_y$) was computed using Eq. (4). For

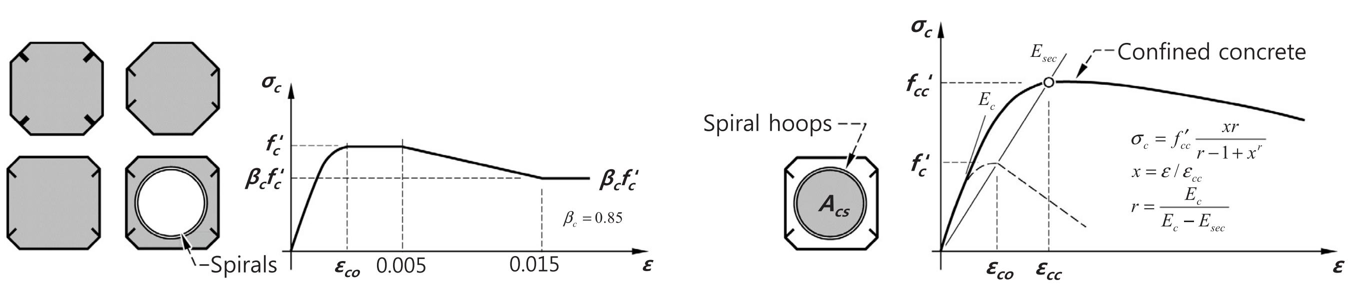

(a) Concrete A_{ct} within octagonal tubes (b) Concrete A_{cs} confined by spiral reinforcement

Fig. 11. Effective stress–strain relationships of concrete accounting for confinement.

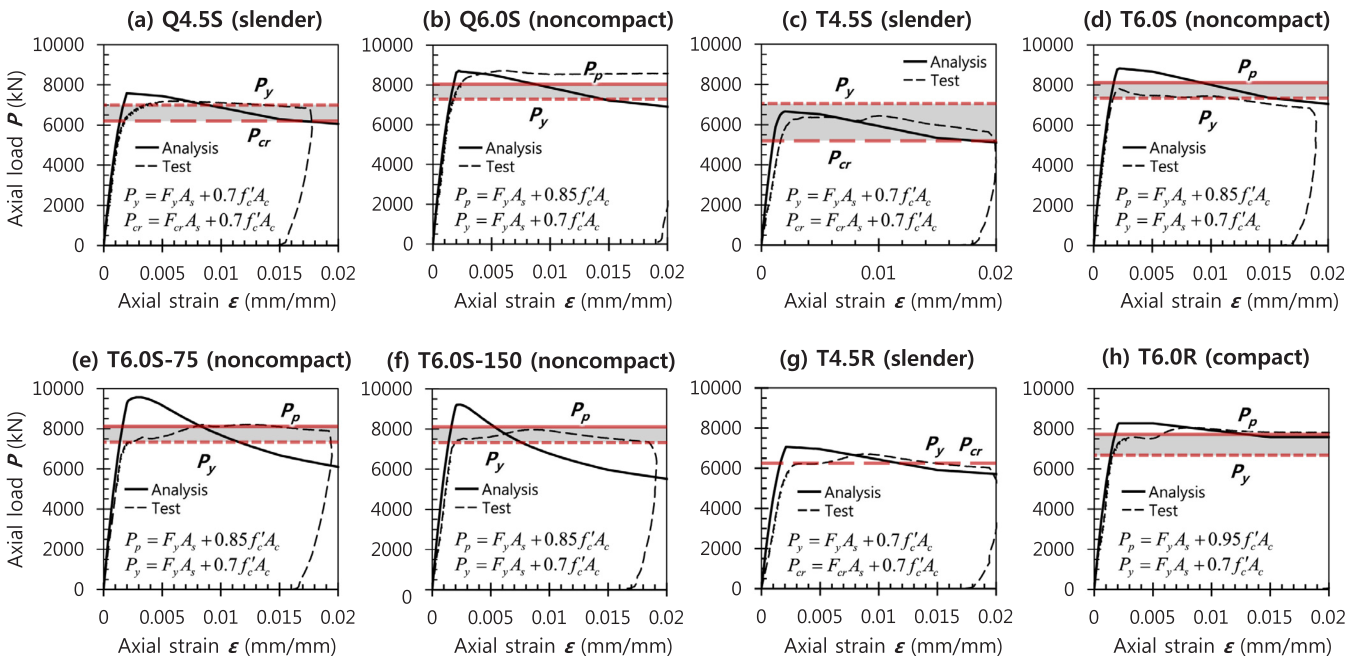

Fig. 12. Comparison of strain-compatibility analysis with test.

T4.5R and T6.0R, with the section geometry close to regular octagon, $C_2 = 0.95$ was used and F_{cr} ($\le F_y$) was computed using Eq. (6).

For Q4.5S, Q6.0S, T4.5S, T4.5R, and T6.0R, the results of the strain compatibility analysis agreed relatively well with the tests. Although differences around the yielding points between the analysis and test were noticeable and the post-yield or post-buckling hardening behavior was not well captured by the analysis, the variation of the compression strengths after the yielding points remained mostly within the shaded bands between P_y and P_{cr} for slender sections, or between P_p and P_y for noncompact and compact sections. However, for T6.0S, T6.0S-75, and T6.0S-150, the maximum strengths predicted by the strain compatibility analysis were much greater than the test strengths, and even greater than the plastic strengths P_p. In particular, for T6.0S-75 and T6.0S-150 using spiral reinforcement inside the tubes, the strength in the region 0.002 mm/mm $\le \varepsilon \le$ 0.005 mm/mm was significantly overestimated, whereas the strength in the region $\varepsilon >$ 0.005 mm/mm was underestimated.

The discrepancy between the analysis and test in Fig. 12 indicates that the effective stress–strain relationships based on the average stresses and strains of the whole steel section need to be improved in the future, considering the following aspects:

(1) For thin-walled tubes with initial imperfection, local buckling begins to occur at a load level less than the theoretical buckling load [20]. This indicates that in Fig. 10, the stress–strain curves for buckled steel tubes, which are sharp at the buckling point, need to be modified as a smooth shape so that gradual transition from linear elastic behavior to post-buckling behavior can be represented.

(2) Since there is no reinforcement for the concrete inside the tube, the concrete strength may not be fully developed after the tube buckles. Thus for slender and noncompact sections, the peak stress of the concrete needs to be less than f_c' (see Eqs. (14) and (15)). For example, Sakino et al. [14] reported that the compressive strength of short CFT columns decreased with increasing column dimension over the size of concrete cylinders used for material strength testing (i.e. 100 mm, scale effects). In fact, the compressive strength of CFT columns is significantly affected by the concrete strength, whereas the flexural or flexure-compression strengths are more affected by the steel tubes. Thus when estimating the axial strength of CFT columns under pure compressive loading, care should be taken not to overestimate the contribution of the concrete. Considering the consistency with the concrete design code such as ACI 318-19 [1], a reduction factor 0.85 for the infilled concrete may be appropriate.

(3) Inside the thin-walled tubes, strength increase due to confinement in the infilled concrete is limited or delayed (refer to the post-yield behavior in Fig. 5(c) and (d)). This is because the thin tube wall with negligible out-of-plane stiffness does not develop confinement until the infilled concrete significantly dilates under large inelastic deformation. Considering that large dilation in the filled concrete occurs only after severe cracking and crushing failure take place, the consequent strength increase in the filled concrete may be limited because strength increase by the confinement is cancelled out by strength loss by the cracking and crushing.

4.4. Compression strength of AISC 360-16

The compressive strength P_{no} of CFT columns can be computed as follows (AISC 360-16):

$$P_{no} = \begin{cases} P_p & \text{for } \lambda \geqslant \lambda_p \\ P_p - \frac{P_p - P_y}{(\lambda_r - \lambda_p)^2}(\lambda - \lambda_p)^2 & \text{for } \lambda_p > \lambda \geqslant \lambda_r \\ P_{cr} & \text{for } \lambda > \lambda_r \end{cases} \tag{16}$$

where λ_p and λ_r are the limits of slenderness ratio for the classification of CFT sections (refer to the footnotes of Table 1). P_p, P_y, and P_{cr} are computed using Eqs. (13)–(15).

Table 2 shows the design strengths P_{no} of the OCFT column specimens. The design strengths are also represented as horizontal lines in Fig. 5. For Q4.5S, Q6.0S, T4.5S, T6.0S, T6.0-75, and T6.0-150, with the section geometry close to square, P_{no} was determined using the AISC 360-16 provisions for square columns. For T4.5R and T6.0R, with the section geometry close to regular octagon, the provisions for circular columns were used, except for F_{cr} computed by Eq. (6). As shown in Table 2, the test-to-design strengths ratios, P_u/P_{no}, were greater than 1.0 for all specimens. The mean and coefficient of variation were 1.09 and 0.044, respectively. This indicates that the existing AISC 360-16 provisions for square and circular CFT columns are applicable to the OCFT columns tested in this study.

Table 2
Design strengths P_{no} by AISC 360-16.

Specimens	P_u (kN)	λ_{eff} 1)	λ_p	λ_r	P_{no} (kN)	P_{no}/P_u
Q4.5S	7,197	68.2	45.7	60.7	6,216	1.16
Q6.0S	8,714	50.7	50.0	66.4	8,018	1.09
T4.5S	6,225	86.9	45.7	60.7	5,210	1.19
T6.0S	7,820	64.7	50.0	66.4	7,526	1.04
T6.0S-75	8,213	64.7	50.0	66.4	7,526	1.09
T6.0S-150	7,969	64.7	50.0	66.4	7,526	1.06
T4.5R 1)	6,707	88.9	61.3	77.7	6,188	1.08
T6.0R 1)	8,064	66.6	73.5	93.1	7,713	1.05

1) P_{no} was computed in accordance with the provisions for circular columns, except for F_{cr}. F_{cr} was computed using Eq. (6) ($\lambda_{eff} = D/t = 180/4.5 = 40$ for T4.5R, and $180/6.0 = 30$ for T6.0R).

5. Summary and conclusions

In this study, the compressive behavior of concrete-filled octagonal thin-walled tube (OCFT) columns were investigated. The conclusions of this study are as follows:

1) Buckling modes and strength were significantly affected by the section geometry and slenderness ratio of the steel tubes. For the T-type octagonal tubes with the section geometry close to a square, buckling modes were similar to those of square tubes. For the Q-type tubes where the corners were fully clamped by the rib plates, the effective width of the tube wall was reduced, and the consequent buckling strength was increased. For regular octagon tubes, buckling modes were similar to those of circular tubes.
2) For all specimens, the octagonal thin-walled tubes underwent elastic or inelastic local buckling. Despite such local buckling, the post-buckling behavior of the OCFT columns was highly ductile. The post-buckling strengths were maintained without degradation, or even increased by the hardening behavior due to concrete confinement.
3) The compression strengths of the OCFT columns were estimated based on the AISC 360-16 provisions for square and circular columns. For the octagonal tubes with the section geometry close to a square, the buckling strength F_{cr} was estimated based on the effective width using the equation for square tubes. For the regular octagon tubes, the theoretical F_{cr} proposed by Susantha et al. [16] was used. The test-to-design strengths ratios were greater than 1.0 for all specimens, and the mean and coefficient of variation were 1.09 and 0.044.
4) A strain compatibility analysis was proposed for the octagonal thin-walled tube columns. For this, effective stress–strain relationships of the steel tube and infilled concrete that accounted for the effects of local buckling and confinement were suggested. Overall, the analysis results agreed reasonably with the tests. However, the strengths at the points of local buckling and yielding were overestimated, and the subsequent post-yield or post-buckling hardening behavior was mostly underestimated.

CRediT authorship contribution statement

Jong-Jin Lim: Investigation, Resources, Writing - original draft. **Tae-Sung Eom:** Conceptualization, Methodology, Investigation, Writing - review & editing.

Declaration of Competing Interest

The authors declare that they have not known competing financial relationships that could have appeared to influence the work reported in this paper.

Acknowledgement

This work was supported by the National Research Foundation of Korea (NRF-2018R1A6A1A07025819), the Urban Architecture Research Program of KAIA (19AUDP-B106327-05), and the National Disaster Management Research Institute (2019-MOIS32-017-01010100-2020), funded by the Korean Government.

Appendix A. Supplementary material

Supplementary data to this article can be found online at https://doi.org/10.1016/j.engstruct.2020.111082.

References

[1] ACI Committee 318. Building Code Requirements for Structural Concrete, ACI 318-19. Farmington Hills (MI): American Concrete Institute; 2019.
[2] American Institute of Steel Construction. Specification for structural steel building. AISC 360-16, Chicago, Illinois; 2016.
[3] Cai J, He ZQ. Axial load behavior of square CFT stub column with binding bars. J Constr Steel Res 2006;62(5):472–83.
[4] Ding F, Li Z, Cheng S, Yu ZW. Composite action of octagonal concrete-filled steel tubular stub columns under axial loading. Thin-Walled Struct 2016;107:453–61.
[5] Fédération Internationale du Béton (fib). fib Model Code for Concrete Structures 2010; 2013.
[6] Ge H, Usami T. Strength of concrete-filled thin-walled steel box columns: experiment. J Struct Eng 1992;118(11):3036–54.
[7] Huang CS, Yeh YK, Liu GY, Hu HT, Tsai KC, Weng YT, et al. Axial load behavior of stiffened concrete-filled steel columns. J Struct Eng 2002;128(9):1222–30.
[8] Jamkhaneh ME, Kafi MA, Kheyroddin A. Behavior of partially encased composite members under various load conditions: experimental and analytical models. Adv Struct Eng 2019;22(1):94–111.
[9] Jamkhaneh ME, Kafi MA. Experimental and numerical study of octagonal composite column subject to various loading. Periodica Polytech Civil Eng 2018;62(2):413–22.
[10] Knowles RB, Park R. Strength of concrete-filled steel tubular columns. J Struct Div ASCE 1969;118(11):3036–54.
[11] Lai Z, Varma AH. Effective stress-strain relationships for analysis of noncompact and slender filled composite (CFT) members. Eng Struct 2016;124:457–72.
[12] Liang QQ, Uy B, Liew JYR. Nonlinear analysis of concrete-filled thin-walled steel box columns with local buckling effects. J Constr Steel Res 2006;62(6):581–91.
[13] Mander JB, Priestley MJ, Park R. Theoretical stress-strain model for confined concrete. J Struct Eng 1988;114(8):1804–26.
[14] Sakino K, Nakahara H, Morino S, Nishiyama I. Behavior of centrally loaded concrete-filled steel-tube short columns. J Struct Eng, ASCE 2004;130(2).
[15] Schneider SP. Axially loaded concrete-filled steel tubes. J Struct Eng, ASCE 1998;124(10):1125–38.
[16] Susantha KAS, Ge Hanbin, Usami T. Uniaxial stress–strain relationship of concrete confined by various shaped steel tubes. Eng Struct 2001;23(10):1331–47.
[17] Tao Z, Han LH, Wang ZB. Experimental behaviour of stiffened concrete-filled thin-walled hollow stee structural (HSS) stub columns. J Constr Steel Res 2005;61(7):962–83.
[18] Tomii M, Ge, Yoshimmra K, Morishita Y. Experimental studies on concrete-filled steel stub columns under concentric loading. In: Proceedings of International Colloquium on Stability of Structures Under Static and Dynamic Loads, SSRC/ASCE/Washington, D.C.; 1977.
[19] Tomii M, Sakino K. Elasto-plastic behavior of concrete filled square steel tubular beam-columns. Trans Arch Inst Japan 1979;280:111–20.
[20] Trahair NS, Bradford MA, Nethercot DA, Gardner L. The behaviour and design of steel structures to EC3 (4th ed). NY, USA: Taylor & Franci; 2008.
[21] Uy B. Local and post-local buckling of concrete filled steel welded box columns. J Constr Steel Res 1998;47(1):47–72.
[22] Uy B, Bradford MA. Elastic local buckling of steel plates in composite steel-concrete members. Eng Struct 1996;18(3):193–200.
[23] Varma AH, Sause R, Ricles JM, Li Q. Development and validation of fiber model for high-strength square concrete-filled steel tube beam-columns. ACI Struct J 2005;120(1):73–84.